Magnetic anisotropy energies and metal-insulator transitions in monolayers of α-RuCl$_3$ and OsCl$_3$ on graphene

P. H. Souza [1,*] D. P. de Andrade Deus [2,†] W. H. Brito [3,‡] and R. H. Miwa [1,§]

[1]*Instituto de Física, Universidade Federal de Uberlândia, C.P. 593, 38400-902, Uberlândia, Minas Gerais, Brazil*
[2]*Instituto Federal de Educação, Ciência e Tecnologia do Triângulo Mineiro, Uberaba, C. P. 1020, 38064-190, Minas Gerais, Brazil*
[3]*Departamento de Física, Universidade Federal de Minas Gerais, C. P. 702, 30123-970, Belo Horizonte, Minas Gerais, Brazil*

Transition metal (TM) trichlorides, with $4d$ or $5d$ electrons, are materials at the forefront of recent studies about the interplay of spin-orbit coupling (SOC) and strong Coulomb interactions. Within our first-principles calculations (DFT $+ U +$ SOC) we study the effects of graphene on the electronic and magnetic properties of the monolayers (MLs) of α-RuCl$_3$ and OsCl$_3$. Despite the spatially inhomogeneous n-type doping induced by graphene, we show that the occupancy of Ru-$4d$ (Os-$5d$) bands of MLs of α-RuCl$_3$(OsCl$_3$) can be tuned through external electric fields and allows the control of (i) metal-insulator transitions and (ii) the magnetic easy-axis and anisotropy energies. Our findings point toward the tuning of electronic and magnetic properties of TM trichloride MLs by using graphene and external electronic fields.

I. INTRODUCTION

Magnetic interactions in correlated materials are well known for giving rise to energy scales and emerging properties. In Mott insulators, with localized d electrons, these interactions can give rise to an antiferromagnetic (AFM) ground state [1,2], which upon hole doping leads to unconventional superconductivity [3]. On the other hand, in f-electron materials, the AFM interaction between local moments and the conduction electrons leads to the Kondo effect and the appearance of strongly renormalized quasiparticles [4]. More recently, the interplay of spin-orbit coupling (SOC), strong Coulomb, and the emerging magnetic interactions has become of great interest since it can give rise to unusual electronic phases and nontrivial topology [5,6].

At the forefront of recent studies in this field are the $4d$- and $5d$-based materials, such as ruthenium and osmium compounds. Particularly α-RuCl$_3$ has attracted great interest since it is a candidate for the realization of a Kitaev-like quantum spin liquid [7]. However, this material is found to be a spin-orbit Mott insulator which orders antiferromagnetically at low temperatures [8]. The intriguing magnetic interactions in α-RuCl$_3$ are also responsible for competing magnetic phases. More recently, authors of several works have addressed the strength and nature of these interactions. For instance, recent x-ray scattering data have obtained a ferromagnetic (FM) Kitaev term in α-RuCl$_3$ [9], in good agreement with previous calculations [10,11]. Moreover, within density functional theory (DFT) $+ U +$ SOC calculations, Kim *et al.* [12] found

that a zigzag (ZZ) AFM phase of α-RuCl$_3$ is slightly more stable than the FM configuration for U values between 1.0 and 3.5 eV, where the former is characterized by an energy gap of $\sim$0.8 eV. Such a nearly degeneracy between FM and ZZ-AFM phases has been confirmed by authors of recent works [13,14].

The monolayers (MLs) of the $4d$ and $5d$ transition metal (TM) trichlorides have also attracted great attention due to their magnetic and electronic properties. Huang *et al.* [13] explored the quantum anomalous Hall (QAH) effect in ML α-RuCl$_3$. However, instead of a semiconducting phase [12], they found a semimetallic system even upon the inclusion of the SOC. In contrast, the semiconducting character of ML α-RuCl$_3$ has been confirmed by recent calculations of Sarikurt *et al.* [15], with energy gaps of $\sim$0.7 eV (FM) and 1.0 eV (ZZ-AFM) for $U = 2.0$ eV. From the experimental side, neutron scattering experiments [16] indicated that single crystals of α-RuCl$_3$, with Ru^{3+} ($4d^5$) ions, exhibit a ZZ-AFM configuration at low temperatures.

Similar magnetic phases have also been explored in ML OsCl$_3$, which in contrast to α-RuCl$_3$ is predicted to be FM [17]. In addition, ML OsCl$_3$ has been considered a candidate for a QAH insulator [17], although the Coulomb interactions counteract and favor the appearance of a Mott insulating phase. More recently, it was pointed out that the parent compound Os$_{0.55}$Cl$_2$ presents features of a quantum spin liquid, with gapless magnetic fluctuations which prevent any magnetic ordering at low temperatures [18]. In addition to the feasibility of layered systems [19] and the prediction of a Hubbard U-dependent QAH phase in ML OsCl$_3$ [17], there are few works exploring its electronic and magnetic properties.

Another interesting property of these two-dimensional (2D) materials is their magnetic anisotropy energy (MAE). In the Ref. [15], the authors reported a MAE of $\sim$18.8 meV with the easy axis parallel to the α-RuCl$_3$ surface.

---
*psouza8628@gmail.com
†dominike@iftm.edu.br
‡walber@fisica.ufmg.br
§hiroki@ufu.br

Further calculations confirmed the energetic preference for the in-plane magnetization; however, they obtained a MAE of 0.80 meV/Ru atom for the ZZ-AFM phase [20], which is much smaller than that obtained in Ref. [15].

Authors of previous reports have also explored different ways to modify the properties of these 2D magnets. In the case of α-RuCl$_3$, strain and optically driven charge excitations can be used to induce magnetic phase transitions [14,20,21]. Another interesting way is by interfacial interaction with graphene. It has been found that the interaction between graphene and ML α-RuCl$_3$ [22] can considerably enhance the Kitaev interactions in the latter, whereas it also modifies the Fermi surface topology of the former [14]. Rizzo *et al.* [23], for instance, found that interlayer charge transfer between ML α-RuCl$_3$ and graphene gives rise to plasmon polaritons with high mobility.

In this paper, we study the electronic and magnetic properties of the MLs of α-RuCl$_3$ and OsCl$_3$ in the presence of graphene (Gr); i.e., α-RuCl$_3$/Gr and OsCl$_3$/Gr heterostructures. We find a net charge transfer (order of magnitude of 10^{13}/cm^2) from graphene to the TM trichlorides, however, inhomogeneously distributed on the α-RuCl$_3$ and OsCl$_3$ surfaces. As a result, Ru-4d (Os-5d) bands of α-RuCl$_3$ (OsCl$_3$) become partially occupied, giving rise to correlated metallic phases. More importantly, we demonstrate that graphene and external electric fields (EEFs) can be used to control the Ru-4d (Os-5d) occupancy and therefore induce (i) metal-insulator transitions and (ii) tune the MAE in both 2D magnets, where the graphene ML acts as a reservoir for the electron/hole doping of the MLs. For instance, in the case of α-RuCl$_3$/Gr, we observe a change of easy axis (from out-of-plane to in-plane) accompanied by an enhancement of the MAE by a factor of six under EEFs of 0.2 eV/Å. These findings suggest that the occupancies of ML α-RuCl$_3$ and OsCl$_3$ bands are essential to control the magnetization easy axis and the corresponding magnetic anisotropic energies. This control can be achieved with the presence of graphene and EEFs.

II. COMPUTATIONAL DETAILS

Our DFT calculations were performed within the Perdew-Burke-Ernzehof generalized gradient approximation [24], using projector augmented wave (PAW) potentials [25], as implemented in the Vienna *Ab initio* Simulation Package (VASP) [26,27]. The structural optimizations were done including van der Waals corrections (vdW-DF) [28] until the forces on each atom were <0.01 eV/Å and total energies are converged within a 1×10^{-6} eV criterion. A plane-wave cutoff of 500 eV was used and k-point meshes of $15 \times 15 \times 1$ and $31 \times 31 \times 1$ for total energy and projected density of states calculations, respectively. The α-RuCl$_3$ and OsCl$_3$ MLs were simulated using a slab with $\sqrt{3} \times \sqrt{3}$ surface periodicity, which corresponds to eight Ru/Os atoms per unit cell [Fig. 1(a)], and a vacuum region of 20 Å separating a slab from its periodic images.

To treat the strong correlations related to electrons within Ru-4d (Os-5d) states, we employed the DFT + U functional of Dudarev *et al.* [29], which considers the electronic interactions at a mean-field level by means of an effective partially screened Coulomb interaction U_{eff}. In this paper, we have
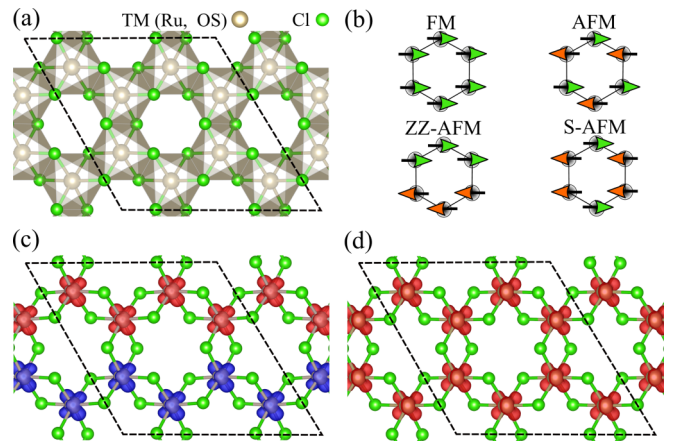

FIG. 1. (a) Layered honeycomb structures of the monolayers of α-RuCl$_3$ and OsCl$_3$. (b) Distinct magnetic configurations associated with Ru(Os) local moments considered in this paper. In (c) and (d), we show the spin density distributions corresponding to zigzag antiferromagnetic (ZZ-AFM) and ferromagnetic (FM) phases of α-RuCl$_3$ and OsCl$_3$, respectively. The red (blue) isosurfaces correspond to spin-up (down) charge densities.

used values of $U_{\text{eff}} = U - J = 1.5$ and 1.0 eV for MLs of α-RuCl$_3$ and OsCl$_3$, respectively [17,22]. The SOC was also considered in our calculations of the electronic and magnetic properties. The calculation of the MAE, defined as the total energy (E) difference of the α-RuCl$_3$ and OsCl$_3$ systems with the magnetization parallel ($\parallel$) and perpendicular ($\perp$) to the slab surface:

$$\text{MAE} = E_{\parallel} - E_{\perp}, \qquad (1)$$

was performed by using the force theorem [30,31] as implemented in VASP code [32].

III. RESULTS AND DISCUSSIONS

A. Electronic and magnetic properties of ML α-RuCl$_3$ and OsCl$_3$ within DFT + U + SOC

MLs of α-RuCl$_3$ and OsCl$_3$ have a 2D honeycomblike structure, with slightly distorted TMCl$_6$ (TM = Ru and Os) edge-sharing octahedra, as shown in Fig. 1(a). The corresponding crystal field splitting and occupancy of the Ru-4d (Os-5d) states lead to well-defined local moments, which can order into distinct magnetic configurations. We performed unconstrained noncolinear DFT + U + SOC calculations to examine the relative energetic stability of several magnetic phases, viz., FM, Neel AFM, ZZ-AFM, and stripy AFM (S-AFM), which are schematically illustrated in Fig. 1(b).

In Table I, we present the obtained total energy differences (ΔE) with respect to the lowest energy configuration, net magnetic moments (M), and bandgaps (E_{gap}) of each magnetic phase. Details of the magnetic orientations are summarized in Table II. We find that ML α-RuCl$_3$ has a semiconducting ZZ-AFM ground state. The corresponding spin density $\Delta \rho^{\text{spin}} = \rho_{\text{up}} - \rho_{\text{down}}$ shows a d_{xy}-shaped $\Delta \rho^{\text{spin}}$ for the ZZ-AFM phase [Fig. 1(c)]. The local moment of $\approx 0.9 \, \mu_{\text{B}}$/Ru atom is in good agreement with previous reports [15,20], though we obtain a distinct ground state magnetic configuration. From our

TABLE I. Relative energetic stabilities ΔE (meV/TM atom) and bandgaps E_{gap} (eV) of distinct magnetic configurations of α-RuCl$_3$ and OsCl$_3$ MLs.

α-RuCl$_3$	ΔE	E_{gap}
ZZ-AFM	0.0	0.74
FM	4.5	0.50
S-AFM	8.6	0.66
AFM	11.6	0.80
OsCl$_3$		
ZZ-AFM	3.0	0.77
FM	0.0	0.54
S-AFM	12.5	0.62
AFM	5.13	0.75

calculations, we find that ZZ-AFM is 4.5 meV/Ru atom more stable than the FM state. By using much the same calculation approach, (i) Sarikurt *et al.* [15] found the FM state as the ground state configuration, with 20 meV/Ru atom more stable than the ZZ-AFM configuration. The authors verified the energetic preference for the FM state for U_{eff} up to 2 eV, whereas for larger values of U_{eff} (2.5 and 3.5 eV), they found that the FM and ZZ-AFM configurations present practically the same total energy. (ii) Collinear magnetic calculations in Ref. [22], using U_{eff} of 1.5 eV, indicate that the FM and ZZ-AFM phases are almost degenerate. Meanwhile, (iii) Kim *et al.* [12] found the ZZ-AFM phase slightly more favorable than the FM phase for U_{eff} between 1.5 and 3.5 eV. Similarly, (iv) Tian *et al.* [14] found an energetic preference for the ZZ-AFM phase for $0 \leqslant U_{eff} \leqslant 5$ eV. (v) Further calculations, using $U_{eff} = 2.0$ eV confirmed the ZZ-AFM phase as the ground state configuration [20]. Those results (i)–(v) were obtained based on first-principles DFT calculations as implemented in different computational codes, namely, VASP [(i), (ii), and (v)]; OPENMX [33] [(iii)]; and QUANTUM ESPRESSO [34] [(iv)]. Additional computational details are presented in Ref. [35].

Moreover, the S-AFM and Neel AFM configurations are ∼9 and 12 meV/Ru less stable than the ZZ-AFM configuration. These small energy differences obtained within our approach reflect the competing energy scales presented in ML α-RuCl$_3$. In fact, as pointed out by Winter *et al.* [36], the rich phase diagram of α-RuCl$_3$ is ruled by competing Coulomb, kinetic, and spin-orbit energy scales as well as long-range

TABLE II. The magnetization module (M) and the Cartesian components M_x, M_y, and M_z (in μ_B/TM atom).

RuCl$_3$	M	M_x	M_y	M_z
ZZ-AFM	0.76	∓0.37	∓0.16	±0.64
FM	0.76	$+0.68$	$+0.33$	$+0.14$
AFM	0.70	±0.02	∓0.02	±0.70
S-AFM	0.77	∓0.05	±0.01	±0.77
OsCl$_3$				
ZZ-AFM	0.45	∓0.45	∓0.03	∓0.00
FM	0.47	$+0.46$	$+0.11$	$+0.02$
AFM	0.19	±0.00	∓0.00	±0.19
S-AFM	0.18	±0.11	±0.00	±0.15

interactions, where the latter are very sensitive to the structural details. It turns out that the ZZ-AFM ground state can be attributed to the presence of a large third-neighbor Heisenberg coupling between the Ru^{3+} local moments. Although ML α-RuCl$_3$ exhibits nearly degenerate magnetic configurations, the insulating nature of the system is preserved. The AFM configurations have larger bandgaps. For instance, ZZ-AFM α-RuCl$_3$ has a bandgap of ∼200 meV larger than the FM configuration.

In the sequence, the energetic preference of the magnetic orientation was evaluated through the calculation of the MAE. We found that ZZ-AFM α-RuCl$_3$ presents an energetic preference for the out-of-plane ($\perp$) magnetization with MAE = 0.163 meV/Ru atom, while the in-plane ($\parallel$) magnetization is more likely in FM α-RuCl$_3$, with MAE = -1.77 meV/Ru atom. Previous studies pointed out an energetic preference for the in-plane magnetization by 18.88 meV [15] and 0.95 meV/Ru atom [20] for FM α-RuCl$_3$ and 0.80 meV/Ru atom [20] for the ZZ-AFM configurations.

As discussed above, the equilibrium geometry plays an important role in the magnetic properties of α-RuCl$_3$. Indeed, we found a subtle commitment between the atomic positions and the preferential orientation of the magnetic moment. We examined six slightly different equilibrium geometries obtained upon small perturbations on the initial (starting) atomic positions and spin configurations. We found that (i) the α-RuCl$_3$ systems with energetic preference for in-plane magnetization (MAE < 0) present Ru-Cl bond lengths (d_{Ru-Cl}) with a nearly uniform distribution, characterized by a deviation ($\sigma_{d_{Ru-Cl}}$) of ∼0.006 Å, whereas (ii) the ones with MAE > 0 present less uniform d_{Ru-Cl} distribution, with $\sigma_{d_{Ru-Cl}} \approx 0.017$ Å. In all cases, we found the lowest energies in (ii) by ∼30 meV/Ru atom when compared with (i), thus providing further support to the energetic preference for the out-of-plane magnetization in α-RuCl$_3$.

In contrast to α-RuCl$_3$, OsCl$_3$ presents a FM ground state followed by the ZZ-AFM configuration, which is higher in energy by 3.0 meV/Os atom; both magnetic phases are characterized by an energetic preference for in-plane magnetization, with a sizable MAE of -27.68 meV/Os atom (FM) and -18.71 meV/Os atom (ZZ-AFM). Our findings are in good agreement with Ref. [17], which reported a small energy difference between the FM and ZZ-AFM configurations and in-plane magnetization. Like α-RuCl$_3$, the spin density of FM OsCl$_3$ is centered around the TM atoms, as can be seen in Fig. 1(d), and possesses a net magnetic moment of 0.9 μ_B/Os atom. The FM ground state exhibits a bandgap of 0.54 eV, while the ZZ-AFM configuration has a gap of 0.77 eV.

The Mott insulating states of α-RuCl$_3$ and OsCl$_3$ MLs are evidenced by the band structures and projected density of states shown in Fig. 2. In both materials, the gap appears due to the splitting of $j_{eff} = \frac{1}{2}$ states which are originated from Ru(Os)-t_{2g} states. Moreover, from the projected density of states, one can notice that states from -1.6 to 1.2 eV are essentially formed by the Ru(Os)-d states, which are gapped due to the interplay of Coulomb repulsion and SOC. In the case of ML OsCl$_3$, we also show the band structure of the ZZ-AFM configuration [Fig. 2(e)] has the same features as RuCl$_3$(ZZ-AFM) [Fig. 2(a)]. The ground states of α-RuCl$_3$ and OsCl$_3$ exhibit bandgaps of 0.74 and 0.54 eV,
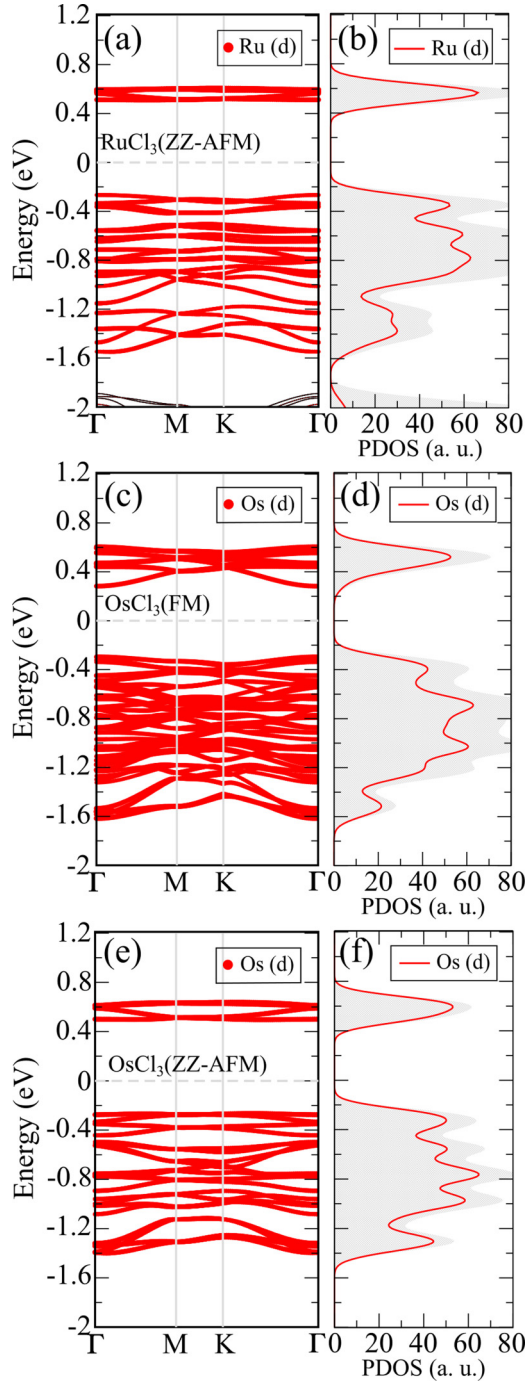
FIG. 2. DFT + U + SOC band structures and projected density of states of the transition metal trichlorides monolayers: (a) and (b) RuCl$_3$ [zigzag antiferromagnetic (ZZ-AFM)], (c) and (d) OsCl$_3$ [ferromagnetic (FM)], and (e) and (f) OsCl$_3$(ZZ-AFM). Red lines represent the contribution from Ru-4d (Os-5d) states. The shaded regions in (b), (d), and (f) correspond to the total density of states.

respectively (see Table I). The former is in good agreement with previous calculations using small U values [22], although photoemission studies for bulk samples indicate values of ∼1.9 eV [37]. It is worth mentioning that, in the case of ML OsCl$_3$, the neglecting of the Hubbard U term leads to
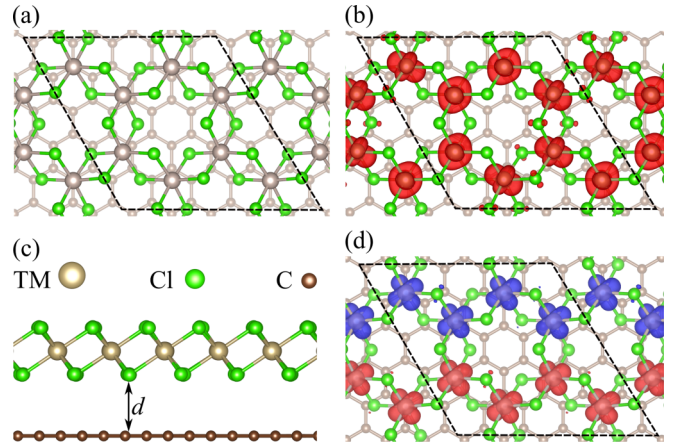

FIG. 3. (a) Optimized structural model of α-RuCl$_3$/Gr and OsCl$_3$/Gr. (b) Spin-resolved charge density isosurface corresponding to ferromagnetic phase of OsCl$_3$/Gr. Similar spin-density is shown in (d) for α-RuCl$_3$/Gr. (c) Side view of our optimized structure, where the interlayer distance $d = 3.6$ Å.

a quantum Hall anomalous insulating state with very small bandgaps of ∼67 meV [17].

B. Effects of graphene on α-RuCl$_3$ and OsCl$_3$

We now address the effects of graphene on the electronic and magnetic properties of both Ru and Os compounds. vdW heterostructures have been employed as an alternative to tailor the properties of 2D materials without any drastic chemical or structural modification. For instance, graphene can be used to enhance the Kitaev interactions and the spin split of bands in ML α-RuCl$_3$ [22,38]. To investigate the energetics and electronic structure of the MLs of α-RuCl$_3$ and OsCl$_3$ on graphene, we perform structural optimizations of lattice parameters considering $\sqrt{3} \times \sqrt{3}$ hexagonal supercells, such as shown in Fig. 3(a). In the optimized structures, the graphene lattice parameter is expanded by 0.84 and 1.68% when interacting with α-RuCl$_3$ and OsCl$_3$, respectively. In contrast, in Ref. [22], the authors kept the graphene lattice parameter fixed, with nearest neighbor distances of 1.42 Å. Moreover, in our optimized structures, the obtained interlayer distance between graphene and α-RuCl$_3$ (OsCl$_3$) is found to be ∼3.6 Å, as illustrated in Fig. 3(b). We evaluate the binding energy of both MLs on graphene as follows:

$$E_b = \frac{E(TMCl_3/Gr) - E(TMCl_3) - E(Gr)}{\text{area}}, \quad (2)$$

where $TM = \{$Ru,Os$\}$. Here, $E(TMCl_3/Gr)$ is the total energy of our optimized structures, whereas $E(TMCl_3)$ denotes the total energy of ML α-RuCl$_3$ (OsCl$_3$). Also, $E(Gr)$ is the total energy of the graphene sheet. We find binding energies of −17.45 and −16.47 meV/Å^2 for α-RuCl$_3$/Gr and OsCl$_3$/Gr, respectively. It is important to mention that binding energy between graphene sheets is around −16.8 meV/Å^2 [39]. These results emphasize the vdW nature of interactions between the TM trichlorides and graphene. Therefore, it is unlikely that heterostructures made of TM trichlorides and graphene exhibit considerable epitaxial in-plane strain values. At the equilibrium geometry, we found that the TM-Cl bond lengths

TABLE III. TM-Cl equilibrium bond length ($d_{TM\text{-}Cl}$) and the respective deviation ($\sigma_{d_{TM\text{-}Cl}}$) of pristine $TM\text{Cl}_3$ ML upon its interaction with graphene, $TM\text{Cl}_3$/Gr. $d_{TM\text{-}Cl}$ and $\sigma_{d_{TM\text{-}Cl}}$ are in Å.

$TM\text{Cl}_3$	$d_{TM\text{-}Cl}$	$\sigma_{d_{TM\text{-}Cl}}$
α-RuCl$_3$(ZZ-AFM)	2.422	0.017
α-RuCl$_3$/Gr (ZZ-AFM)	2.421/2.432	0.018
OsCl$_3$(FM)	2.429	0.004
OsCl$_3$/Gr (ZZ-AFM)	2.412/2.420	0.016

TABLE IV. Bader charges [in units of e/unit cell ($\sqrt{3} \times \sqrt{3}$)] of isolated α-RuCl$_3$ (OsCl$_3$) and heterostructures with graphene. δ denotes the difference between the obtained charges of each isolated ML and in presence of graphene.

Atom	Charge (isolated)	Charge (on graphene)	δ
		α-RuCl$_3$	
Ru	53.73	53.88	0.15
Cl	178.18	178.45	0.27
		OsCl$_3$	
Os	52.91	53.00	0.09
Cl	179.01	179.19	0.18

($d_{TM\text{-}Cl}$) are slightly modified due to the Gr $\rightarrow TM\text{Cl}_3$ net charge transfer (discussed below) and the respective formation of interface dipole. Our results of $d_{TM\text{-}Cl}$ in $TM\text{Cl}_3$ and $TM\text{Cl}_3$/Gr are summarized in Table III.

Next, we address the charge transfer between graphene and ML α-RuCl$_3$ (OsCl$_3$) by calculating the Bader charges of the heterostructures and the isolated systems as well. Our results are displayed in Table IV. According to our findings, graphene donates 3.2×10^{13} e/cm^2 to α-RuCl$_3$ and 2.1×10^{13} e/cm^2 to OsCl$_3$. Roughly speaking, these results can be explained by the deep work functions (Φ) of the TM trichlorides, which are 6.10 and 5.51 eV for single-layer α-RuCl$_3$ and OsCl$_3$, respectively, whereas $\Phi = 4.6$ eV for graphene [23].

In Fig. 4, we display the associated charge transfer map given by $\Delta\rho = \rho(TM\text{Cl}_3/\text{Gr}) - [\rho(TM\text{Cl}_3) + \rho(\text{Gr})]$, with $TM = \{\text{Ru, Os}\}$. In agreement with the obtained Bader charges, we find that graphene donates electrons to the TM thrichloride MLs. Indeed, p-type doping of graphene in contact with α-RuCl$_3$ has been experimentally observed, and supported by first-principles DFT calculations [22,38,40,41]. More interestingly, we observe an inhomogeneous electron doping of both α-RuCl$_3$ and OsCl$_3$, which is more pronounced in the former [Fig. 4(a)]. Such inhomogeneous doping can be explained by the different hoppings between the $TM\text{Cl}_3$ ML and the π orbitals of the graphene sheet, which are sensitive to the stacking geometry at the α-RuCl$_3$/Gr and OsCl$_3$/Gr interfaces. According to Ref. [42], the G peak in Raman spectroscopy data does not shift in α-RuCl$_3$/Gr,

indicating a homogeneous doping. However, electronic transport measurements [43] reported on the existence of lightly or highly doped regions in α-RuCl$_3$/G, which were used to interpret their transport data. As we will show later, our calculations reveal that the Ru atoms in α-RuCl$_3$/G present a finite electronic density of states around the Fermi level, which is in agreement with metallic dI/dV spectra obtained by scanning tunneling spectroscopy of single-layer α-RuCl$_3$/graphite [40]. It is important to mention that inhomogeneous charge doping can be deleterious to the charge carrier transport in those systems, for instance, through the formation of electron-hole puddles [44,45], and have important effects on the magnetic interactions between the TM atoms within the distinct charge domains. It is worth noting that such an inhomogeneous net charge distribution, although less intense, has also been observed in OsCl$_3$/Gr, Fig. 4(b).

The interaction with graphene also gives rise to important effects on the electronic and magnetic properties of the TM trichlorides. As can be seen in Figs. 5(a) and 5(c), the donated electrons occupy the narrow bands of both α-RuCl$_3$ and OsCl$_3$, giving rise to correlated metallic phases. As a result, the graphene Dirac cone appears $\sim$0.6 eV (0.5 eV) above the Fermi level in α-RuCl$_3$ (OsCl$_3$)/Gr, in good agreement with previous reports [22,23]. This can be observed in our calculated projected density of states shown in Figs. 5(b)
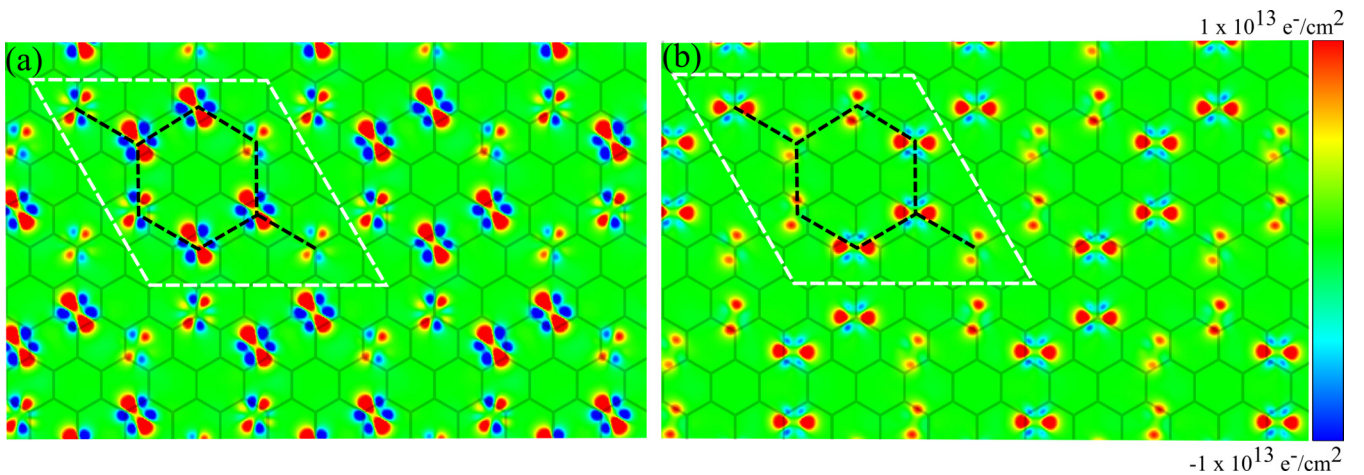

FIG. 4. In-plane $\Delta\rho$ cut of isosurface associated with charge transfer from graphene to (a) α-RuCl$_3$ and (b) OsCl$_3$ monolayers. White dashed lines represent the supercells employed in our calculations. Black dashed lines show the hexagonal Ru and Os lattice to (a) α-RuCl$_3$ and (b) OsCl$_3$.
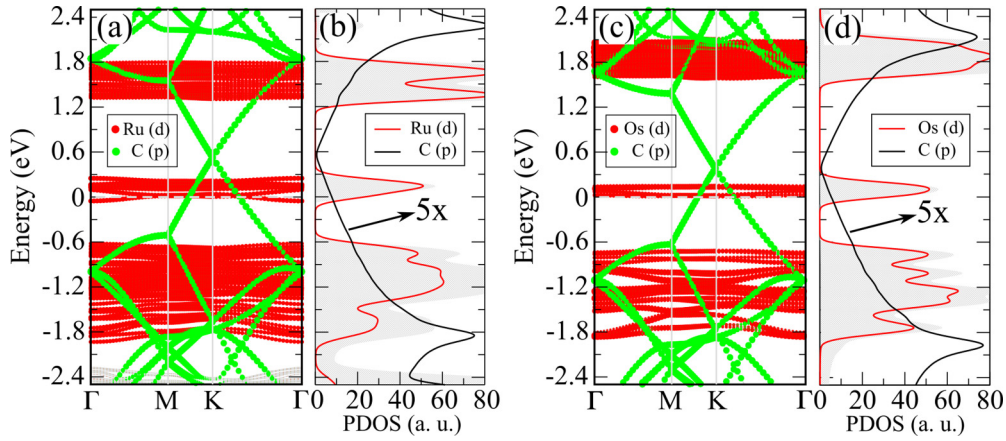
FIG. 5. Orbital resolved band structures and projected density of states of (a) and (b) α-RuCl$_3$/Gr and (c) and (d) OsCl$_3$/Gr. The Ru-4d (Os-5d) states are shown in red, whereas C-2p states are shown in green.

and 5(d), where one can also notice the doping of the Ru-4d (Os-5d) bands. In addition to the (partial) occupancy of these bands, there is also a downshift of the high-energy Ru(Os)-e_g-like states in the presence of graphene. In fact, these states downshift by ~0.40 eV in α-RuCl$_3$ and 0.36 eV in OsCl$_3$.

Focusing on the magnetic properties, we found that the ground state configuration of α-RuCl$_3$, namely, the ZZ-AFM phase with out-of-plane magnetization, remains the same in α-RuCl$_3$/Gr. However, the total energy difference between the ZZ-AFM and FM configurations increases from 4.5 to 26.2 meV/Ru atom, thus indicating that the energetic preference for the ZZ-AFM phase has been strengthened in α-RuCl$_3$/Gr. Meanwhile, there is a slight reduction of the MAE from 0.163 to 0.118 meV/Ru atom. On the other hand, in OsCl$_3$/Gr, the ground state configuration of OsCl$_3$ changes from FM to ZZ-AFM, where the latter becomes more stable than the former by 8.19 meV/Os atom. In both cases, the energetic preference for the in-plane magnetization is maintained; however, somewhat like its counterpart α-RuCl$_3$/Gr, there is a reduction of the MAE, viz., $-27.68 \rightarrow -15.17$ meV/Os atom (FM phase), and $-18.71 \rightarrow -14.04$ meV/Os atom (ZZ-AFM). Since the structural changes on the α-RuCl$_3$ and OsCl$_3$ MLs due to their interaction with the graphene sheet are nearly negligible, we can infer that these changes (on the magnetic properties) are mostly dictated by the net charge transfer between graphene and the TM trichlorides. The role played by the Gr $\leftrightarrow$ TMCl$_3$ charge transfers will be discussed in the next subsection.

As pointed out by Wang et $al.$ [46], the MAE depends on the relative position of occupied and unoccupied d energy levels and on the coupling between them through the angular momentum operator **L**. According to the authors, based on the second-order perturbation theory, the MAE can be estimated as follows:

$$\text{MAE} \approx \xi^2 \sum_{o,u} \left(\frac{|\langle o|L_z|u\rangle|^2 - |\langle o|L_x|u\rangle|^2}{\epsilon_u - \epsilon_o} \right), \quad (3)$$

for in-plane (out-of-plane) magnetization along the x (z) direction. Here, ϵ_u and ϵ_o are the eigenvalues of the corresponding eigenstates, unoccupied (u) and occupied (o), and ξ is the amplitude to the SOC. Based on the equation above, combined

with the orbital projected DFT + U + SOC results [32], we can have a detailed understanding of the MAE results upon the formation of α-RuCl$_3$/Gr and OsCl$_3$/Gr interfaces [47,48].

Our orbital resolved MAE results, as displayed in Fig. 6, reveal that the out-of-plane magnetization of α-RuCl$_3$ is mostly dominated by the in-plane Ru-4d orbitals via the matrix element corresponding to a MAE of 1.27 meV/Ru atom, but there is also a contribution from out-of-plane orbitals $\langle d_{z^2}|L_x|d_{yz}\rangle$ favoring the in-plane magnetization. As shown in Fig. 6(a), the values of the former term are larger than the latter one by 0.490 meV/Ru atom. This energy difference between the matrix elements reduces to 0.413 meV/Ru atom in α-RuCl$_3$/Gr [Fig. 6(b)], which is consistent with the reduction of MAE discussed above. The OsCl$_3$ and OsCl$_3$/Gr systems present a somewhat similar picture, where the matrix element $\langle d_{z^2}|L_x|d_{yz}\rangle$ dictates the energetic preference for in-plane magnetization, which in its turn reduces (by ~6.6 meV/Os
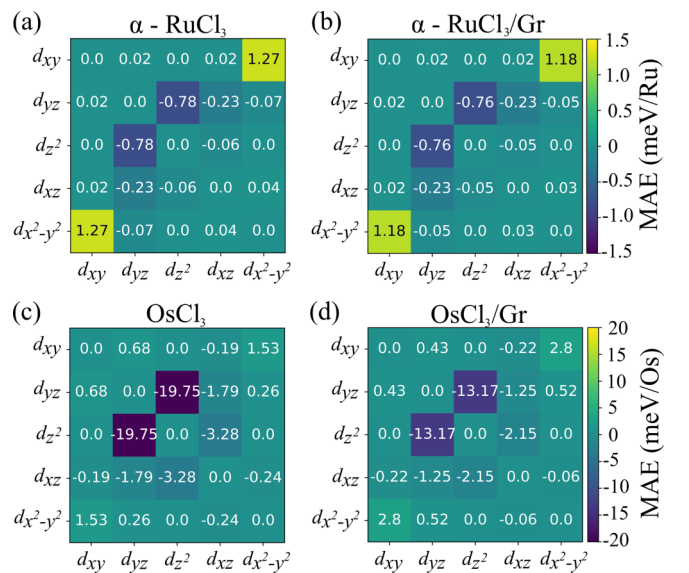

FIG. 6. Orbital resolved magnetic anisotropy energies (in meV/TM atom) for (a) α-RuCl$_3$, (b) α-RuCl$_3$/Gr, (c) OsCl$_3$, and (d) OsCl$_3$/Gr. The blocks in our plots emphasize the contribution of the corresponding matrix elements.
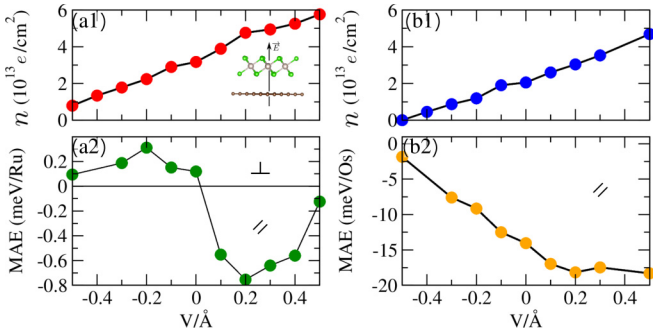
FIG. 7. Electron charge transfer as a function of an external electric field for (a) $RuCl_3$/Gr and (b) $OsCl_3$/Gr. The direction of the external field is illustrated in the inset of (a1). In (a2) and (b2), we show the obtained magnetic anisotropy energies (MAEs) for α-$RuCl_3$/Gr and $OsCl_3$/Gr, respectively. The parallel ($\parallel$) and perpendicular ($\perp$) to the surface magnetizations are also indicated.

FIG. 8. Band structures of (a) α-$RuCl_3$/Gr and (b) $OsCl_3$/Gr, in the presence of external electric fields of -0.8 and -0.5 V/Å, respectively. Bands shown in black (red) denote the calculated band structures without (with) an external electric field.

atom) in the presence a graphene sheet, as shown in Figs. 6(c) and 6(d).

C. Electric-field-induced metal-insulator transitions and control of magnetic anisotropy

The suitable control of the electronic and magnetic properties of materials by external agents, like mechanical pressure and electric field, is an important issue for the development of electronic devices, for instance, metal-insulator switching in TM oxides and intermetallic compounds [49–51], band alignment [52–54], control of the magnetic phases [55,56] in 2D materials mediated by EEFs and mechanical pressure [57,58]. In the case of the α-$RuCl_3$/Gr and $OsCl_3$/Gr heterostructures, in addition to the Gr $\rightarrow TMCl_3$ electron doping (discussed above), we have also examined the effect of EEFs on the control of the net charge transfers and on the magnetic/electronic properties as well [59]. We mention that the electric fields considered here can be obtained in STM experiments with tip-sample distances of $\sim$10 Å [40].

As shown in Figs. 7(a1) and 7(b1), α-$RuCl_3$/Gr and $OsCl_3$/Gr heterostructures present nearly linear behavior of charge transfer as a function of the EEF. The n-type doping of the $TMCl_3$ MLs decreases upon negative values of EEF. For an EEF of ~ -0.65 eV/Å, the electron transfer from graphene to α-$RuCl_3$ has been suppressed; likewise, such a suppression occurs for an EEF of ~ -0.50 eV/Å in the case of $OsCl_3$/Gr. In the opposite direction, one can increase the electron doping of $TMCl_3$ MLs mediated by positive values of the EEF. For instance, for an EEF of 0.3 eV/Å we find an electron doping of the α-$RuCl_3$ and $OsCl_3$ MLs of $\sim$5.0 $\times 10^{13}$ and 3.5 $\times 10^{13}$ e/cm^2, respectively. Therefore, the occupancy of α-$RuCl_3$ and $OsCl_3$ can be controlled by the EEF, as can be seen in the band structures shown in Figs. 8(a) and 8(b). We observe insulating phases for α-$RuCl_3$ and $OsCl_3$ upon EEFs of -0.7 and -0.5 eV/Å, respectively. The suppression of the charge transfers also leads to considerable downshift of the Dirac cone of graphene, as expected. As a result, occupancy-driven metal-insulator transitions in α-$RuCl_3$ ($OsCl_3$) can be induced through EEFs. Thus, our results demonstrate an alternative way to tune the 4d and 5d
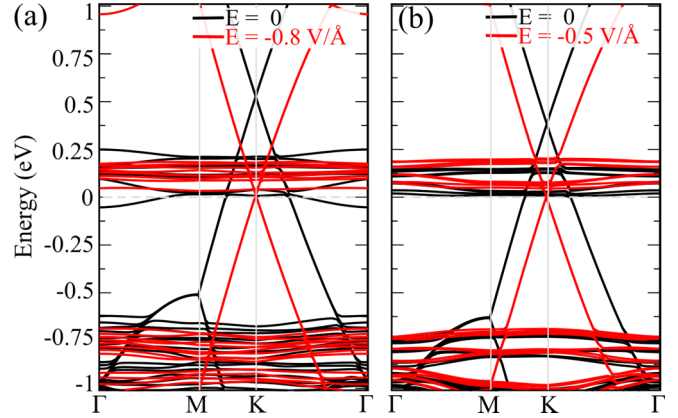
band filling in these compounds and the magnetic properties of the $TMCl_3$ systems. Indeed, as shown in Figs. 7(a2) and 7(b2), the MAE of $TMCl_3$/Gr can be tuned by the EEF.

In Fig. 7(a2), we present the MAE of $RuCl_3$/Gr as a function of the EEF. It is noticeable that, (i) within $|EEF| \leqslant 0.5$ eV/Å, the strength of the out-of-plane magnetization increases from 0.118 meV/Ru atom (EEF $= 0$) to 0.311 meV/Ru atom for an EEF of -0.2 eV/Å, corresponding to a reduction of the Gr $\rightarrow RuCl_3$ charge transfer $\Delta\rho$ from 3.2 $\times 10^{13}$ to 2.2 $\times 10^{13}$ e/cm^2. In contrast, (ii) the in-plane magnetization becomes energetically more favorable for positive values of the EEF, where we found MAE of -0.754 meV/Ru atom for an EEF of 0.2 eV/Å. In this case, the n-type doping of $RuCl_3$ increases with $\Delta\rho$ of 4.8×10^{13} e/cm^2.

We can gain further understanding of the role played by the EEF by analyzing its effect on the (DFT $+ U$) orbital contribution to the MAE, Eq. (2). Overall, we find that the orbital contributions to the MAE are reduced in comparison with those with no EEF. For instance, the out-of-plane contribution given by the matrix element $\langle d_{x^2-y^2} |L_z| d_{xy} \rangle$ reduces from 1.176 to 0.891 meV/Ru atom, while the in-plane contribution via $\langle d_{z^2} |L_x| d_{yz} \rangle$ reduces (in absolute values) from 0.763 to 0.445 meV/Ru atom. The larger energy reduction of the latter matrix element leads to an energetic preference for the out-of-plane magnetization, as discussed in (i). On the other hand, for an EEF of 0.2 eV/Å [(ii)], the preference for in-plane magnetization, MAE $= -0.754$ meV/Ru atom, is mostly ruled by the matrix element $\langle d_{x^2-y^2} |L_z| d_{xy} \rangle$ integrated over orbitals with opposite spins [46,47].

Meanwhile, the energetic preference for in-plane magnetization in $OsCl_3$/Gr is maintained within $|EEF| \leqslant 0.5$ eV/Å, Figure 7(b2). There is an increase of the MAE from -14.04 meV/Os atom (EEF $= 0$) to -18.16 meV/Os atom for EEF $= 0.2$ eV/Å; in the opposite direction, we find a nearly linear reduction of the MAE, $-14.04 \rightarrow -1.84$ meV/Os atom, for negative values of EEF from 0 to -0.5 eV/Å. In the latter limit, the net charge transfer from graphene to $OsCl_3$ is suppressed, $\Delta\rho = 0$, suggesting that the preferential magnetization can

be tuned from in-plane to out-of-plane mediated by higher values of EEF or *p*-type doping of the OsCl$_3$ ML. We have also examined the effect of EEF on the MAE in light of the perturbation theory. The calculated matrix elements are presented in Eq. (2), for EEF = 0.2 and −0.5 eV/Å, respectively, where we show that the MAE changes as a function of the EEF are mostly ruled by the matrix elements $\langle d_{z^2} |L_x| d_{yz} \rangle$ and $\langle d_{z^2} |L_x| d_{xz} \rangle$. For instance, contribution from the former element increases/decreases from −13.165 (EFF = 0) to −15.139/−3.99 meV/Os atom for an EEF of 0.2/−0.5 eV/Å.

It is worth noting that the changes in the MAE as a function of the EEF are dictated by the occupation of the Ru-4*d* and Os-5*d* states, which are resonant or nearly resonant to the Dirac point. Thus, to stress the importance of the Ru-4*d* and Os-5*d* bands on the magnetization direction, we calculated the MAE of *n*-type (*p*-type) doped ML α-RuCl$_3$ (OsCl$_3$). We found a magnetic transition from out-of-plane to in-plane, MAE = 0.163 → −0.213 meV/Ru atom for *n* = 1 *e*, in accordance with the energetic preference for the in-plane magnetization of α-RuCl$_3$/Gr upon EEF > 0 [Fig. 7(a2)]. Meanwhile, we find MAE = −16.41 meV/Os atom in the *p*-type doped (*p* = 0.033 *h* upon an EEF of −0.7 eV/Å) OsCl$_3$ ML, confirming the tendency of change on the magnetic orientation, in-plane → out-of-plane, for EEF < −0.5 eV/Å [Fig. 7(b2)]. Thus, our findings based on electron and hole doping of α-RuCl$_3$ and OsCl$_3$ MLs, respectively, provide strong evidence that the occupation of the Ru-4*d* (Os-5*d*) states, indeed, play an important role on the tuning of the MAE.

IV. SUMMARY AND CONCLUSIONS

In summary, we performed DFT + *U* + SOC calculations to investigate the effects of graphene on the electronic and magnetic properties of MLs of α-RuCl$_3$ and OsCl$_3$, i.e., α-RuCl$_3$/Gr and OsCl$_3$/Gr heterostructures. We find that α-RuCl$_3$ and OsCl$_3$ MLs become *n*-type doped, with *n* of the order of 10^{13} *e*/cm^2, characterized by an inhomogeneous spatial distribution of the net charge density, which depends on the stacking geometry (orbital hopping) between Ru (Os) and carbon atoms. The corresponding charge transfer gives rise to correlated metallic phases in both materials, mediated by the partially occupied Ru-4*d* (Os-5*d*) bands. We demonstrate that metal-insulator transitions can be induced in α-RuCl$_3$/Gr and OsCl$_3$/Gr using EEFs, which in turn controls the occupancy of the Ru-4*d* and Os-5*d* states. More important, such control on the occupancies leads to tuneable magnetic properties. We found that the in-plane magnetization becomes more energetically favorable than the out-of-plane one in α-RuCl$_3$ upon *n*-type doping. Meanwhile, in the opposite direction, *p*-type

doping of OsCl$_3$ results in an in-plane → out-of-plane transition in the preferential magnetization direction. Our findings suggest that the occupancies of Ru-4*d* (Os-5*d*) bands of the TM trichlorides are the key ingredients to tune the magnetic easy axis as well as the MAEs in these 2D correlated materials. This tuning can be achieved with graphene and EEFs.

APPENDIX: MATRIX ELEMENTS OF THE ORBITAL RESOLVED MAE

To calculate the MAE, we performed DFT + *U* + SOC calculations with the zeroth-order approximation for the SOC, where [32]

$$H_{\text{soc}}^{\alpha\beta} = \frac{\hbar^2}{(2m_e c)^2} \frac{K(r)}{r} \frac{dV(r)}{dr} \vec{\sigma}^{\alpha\beta} \vec{L}, \qquad \text{(A1)}$$

where $\vec{L} = \vec{r} \times \vec{p}$ is the angular momentum operator, and $\vec{\sigma}^{\alpha\beta} = (\sigma_x, \sigma_y, \sigma_z)$ are the Pauli spin matrices. Within the PAW methodology, the potential

$$K(r) = \left[1 - \frac{V(r)}{2m_e c^2}\right]^{-2}, \qquad \text{(A2)}$$

where $V(r)$ is the spherical part of the effective all-electron potential within the PAW sphere [32]. Therefore, the matrix elements presented in Sec. III A were calculated as follows:

$$E_{\text{soc}}^{ij} = \delta_{\mathbf{R}_i \mathbf{R}_j} \delta_{l_i l_j} \sum_{n\mathbf{k}} w_{\mathbf{k}} f_{n\mathbf{k}}$$
$$\times \sum_{\alpha\beta} \langle \tilde{\psi}_{n\mathbf{k}}^{\alpha} | \tilde{p}_i \rangle \langle \phi_i | H_{\text{soc}}^{\alpha\beta} | \phi_j \rangle \langle \tilde{p}_j | \tilde{\psi}_{n\mathbf{k}}^{\beta} \rangle, \qquad \text{(A3)}$$

where $\phi_i(\mathbf{r}) = R_i(|\mathbf{r} - \mathbf{R}_i|) Y_{l_i m_i}(\mathbf{r} - \mathbf{R}_i)$ are the partial waves of an atom centered at $\mathbf{R}_i$, $\tilde{\psi}_{n\mathbf{k}}^{\alpha}$ is the spinor component α of the pseudo-orbital with band index *n* and Bloch vector *k*, $f_{n\mathbf{k}}$ and $w_{\mathbf{k}}$ are the Fermi and *k*-point weights, respectively, and $\tilde{p}_i$ are the PAW projector functions.

We emphasize that the VASP implementation allow us to control the spin quantization axis in such way that one can evaluate the matrix elements of H_{soc} for in-plane and out-of-plane magnetization. In our case, we evaluated it for *l* = 2, i.e., for partial waves associated with Ru(Os)-*d* states.

[1] N. F. Mott, *Metal-Insulator Transitions*, 2nd ed. (CRC Press, London, 1990).

[2] P. W. Anderson, Antiferromagnetism. theory of superexchange interaction, Phys. Rev. **79**, 350 (1950).

[3] P. A. Lee, N. Nagaosa, and X.-G. Wen, Doping a Mott insulator: physics of high-temperature superconductivity, Rev. Mod. Phys. **78**, 17 (2006).

[4] P. Coleman, *Heavy fermions: electrons at the edge of magnetism, in Handbook of Magnetism and Advanced Magnetic Materials: Fundamentals and Theory*, edited by H. Kronmuller and S. Parkin (John Wiley and Sons, New York, 2007), Vol. 1.

[5] W. Witczak-Krempa, G. Chen, Y. B. Kim, and L. Balents, Correlated quantum phenomena in the strong spin-orbit regime, Annu. Rev. Condens. Matter Phys. **5**, 57 (2014).

[6] J. G. Rau, E. K.-H. Lee, and H.-Y. Kee, Spin-orbit physics giving rise to novel phases in correlated systems: Iridates and related materials, Annu. Rev. Condens. Matter Phys. **7**, 195 (2016).

[7] L. J. Sandilands, Y. Tian, K. W. Plumb, Y.-J. Kim, and K. S. Burch, Scattering Continuum and Possible Fractionalized Excitations in α-RuCl$_3$, Phys. Rev. Lett. **114**, 147201 (2015).

[8] K. W. Plumb, J. P. Clancy, L. J. Sandilands, V. V. Shankar, Y. F. Hu, K. S. Burch, H.-Y. Kee, and Y.-J. Kim, α-RuCl$_3$: A spin-orbit assisted Mott insulator on a honeycomb lattice, Phys. Rev. B **90**, 041112(R) (2014).

[9] J. A. Sears, L. E. Chern, S. Kim, P. J. Bereciartua, S. Francoual, Y. B. Kim, and Y.-J. Kim, Ferromagnetic Kitaev interaction and the origin of large magnetic anisotropy in α-RuCl$_3$, Nat. Phys. **16**, 837 (2020).

[10] S. M. Winter, K. Riedl, P. A. Maksimov, A. L. Chernyshev, A. Honecker, and R. Valentí, Breakdown of magnons in a strongly spin-orbital coupled magnet, Nat. Commun. **8**, 1152 (2017).

[11] P. A. Maksimov and A. L. Chernyshev, Rethinking α-RuCl$_3$, Phys. Rev. Res. **2**, 033011 (2020).

[12] H.-S. Kim, V. Vijay Shankar, A. Catuneanu, and H.-Y. Kee, Kitaev magnetism in honeycomb RuCl$_3$ with intermediate spin-orbit coupling, Phys. Rev. B **91**, 241110(R) (2015).

[13] C. Huang, J. Zhou, H. Wu, K. Deng, P. Jena, and E. Kan, Quantum anomalous Hall effect in ferromagnetic transition metal halides, Phys. Rev. B **95**, 045113 (2017).

[14] Y. Tian, W. Gao, E. A. Henriksen, J. R. Chelikowsky, and L. Yang, Optically driven magnetic phase transition of monolayer RuCl$_3$, Nano Lett. **19**, 7673 (2019).

[15] S. Sarikurt, Y. Kadioglu, F. Ersan, E. Vatansever, O. Üzengi Aktürk, Y. Yüksel, Ü. Aklncl, and E. Aktürk, Electronic and magnetic properties of monolayer α-RuCl$_3$: A first-principles and Monte Carlo study, Phys. Chem. Chem. Phys. **20**, 997 (2018).

[16] J. A. Sears, M. Songvilay, K. W. Plumb, J. P. Clancy, Y. Qiu, Y. Zhao, D. Parshall, and Y.-J. Kim, Magnetic order in α-RuCl$_3$: A honeycomb-lattice quantum magnet with strong spin-orbit coupling, Phys. Rev. B **91**, 144420 (2015).

[17] X.-L. Sheng and B. K. Nikolić, Monolayer of the 5d transition metal trichloride OsCl$_3$: A playground for two-dimensional magnetism, room-temperature quantum anomalous Hall effect, and topological phase transitions, Phys. Rev. B **95**, 201402(R) (2017).

[18] M. A. McGuire, Q. Zheng, J. Yan, and B. C. Sales, Chemical disorder and spin-liquid-like magnetism in the van der Waals layered 5d transition metal halide Os$_{0.55}$Cl$_2$, Phys. Rev. B **99**, 214402 (2019).

[19] M. Grönke, P. Schmidt, M. Valldor, S. Oswald, D. Wolf, A. Lubk, B. Büchner, and S. Hampel, Chemical vapor growth and delamination of α-RuCl$_3$ nanosheets down to the monolayer limit, Nanoscale **10**, 19014 (2018).

[20] F. Iyikanat, M. Yagmurcukardes, R. T. Senger, and H. Sahin, Tuning electronic and magnetic properties of monolayer α-RuCl$_3$ by in-plane strain, J. Mater. Chem. C **6**, 2019 (2018).

[21] D. A. S. Kaib, S. Biswas, K. Riedl, S. M. Winter, and R. Valentí, Magnetoelastic coupling and effects of uniaxial strain in α-RuCl$_3$ from first principles, Phys. Rev. B **103**, L140402 (2021).

[22] S. Biswas, Y. Li, S. M. Winter, J. Knolle, and R. Valentí, Electronic Properties of α-RuCl$_3$ in Proximity to Graphene, Phys. Rev. Lett. **123**, 237201 (2019).

[23] D. J. Rizzo, B. S. Jessen, Z. Sun, F. L. Ruta, J. Zhang, J.-Q. Yan, L. Xian, A. S. McLeod, M. E. Berkowitz, K. Watanabe *et al.*, Charge-transfer plasmon polaritons at graphene/α-RuCl$_3$ interfaces, Nano Lett. **20**, 8438 (2020).

[24] J. P. Perdew, K. Burke, and M. Ernzerhof, Generalized Gradient Approximation Made Simple, Phys. Rev. Lett. **77**, 3865 (1996).

[25] P. E. Blöchl, Projector augmented-wave method, Phys. Rev. B **50**, 17953 (1994).

[26] G. Kresse and J. Furthmüller, Efficiency of *ab-initio* total energy calculations for metals and semiconductors using a plane-wave basis set, Comput. Mater. Sci. **6**, 15 (1996).

[27] G. Kresse and J. Furthmüller, Efficient iterative schemes for *ab initio* total-energy calculations using a plane-wave basis set, Phys. Rev. B **54**, 11169 (1996).

[28] M. Dion, H. Rydberg, E. Schröder, D. C. Langreth, and B. I. Lundqvist, Van der Waals Density Functional for General Geometries, Phys. Rev. Lett. **92**, 246401 (2004).

[29] S. L. Dudarev, G. A. Botton, S. Y. Savrasov, C. J. Humphreys, and A. P. Sutton, Electron-energy-loss spectra and the structural stability of nickel oxide: An LSDA $+U$ study, Phys. Rev. B **57**, 1505 (1998).

[30] M. Weinert, R. E. Watson, and J. W. Davenport, Total-energy differences and eigenvalue sums, Phys. Rev. B **32**, 2115 (1985).

[31] X. Wang, D.-s. Wang, R. Wu, and A. Freeman, Validity of the force theorem for magnetocrystalline anisotropy, J. Magn. Magn. Mater. **159**, 337 (1996).

[32] S. Steiner, S. Khmelevskyi, M. Marsmann, and G. Kresse, Calculation of the magnetic anisotropy with projected-augmented-wave methodology and the case study of disordered Fe$_{1-x}$Co$_x$ alloys, Phys. Rev. B **93**, 224425 (2016).

[33] T. Ozaki, Variationally optimized atomic orbitals for large-scale electronic structures, Phys. Rev. B **67**, 155108 (2003).

[34] P. Giannozzi, S. Baroni, N. Bonini, M. Calandra, R. Car, C. Cavazzoni, D. Ceresoli, G. L. Chiarotti, M. Cococcioni, I. Dabo *et al.*, QUANTUM ESPRESSO: a modular and open-source software project for quantum simulations of materials, J. Phys.: Condens. Matter **21**, 395502 (2009).

[35] In (i), DFT $+U+$ SOC calculations, Kohn-Sham orbitals (KS) expanded in a plane-wave basis-set with energy cutoff (E_c) of 400 eV, and k-point grid (k_{grid}) of ($18 \times 8 \times 1$); in (ii) DFT $+U$ calculations, with $E_c = 600$ eV, and k_{grid} of ($6 \times 6 \times 1$) for the structural relaxation, and total energy calculations, followed by DFT $+U+$ SOC for the electronic structure calculations, and $k_{grid} = 1000$ points to extract the magnetic interaction parameters; in (iii), DFT $+U+$ SOC calculation with k_{grid} of ($8 \times 8 \times 1$), and linear combination of the pseudoatomic orbitals for the KS basis set; in (iv), DFT $+U+$ SOC calculations with $k_{grid} = (6 \times 3 \times 1)$; and in (v), DFT $+U$ with k_{grid} of ($7 \times 4 \times 1$) for

the structural relaxations and total energy calculations, and (15 $\times$ 9 $\times$ 1) for the electronic structure calculations.

[36] S. M. Winter, Y. Li, H. O. Jeschke, and R. Valentí, Challenges in design of Kitaev materials: magnetic interactions from competing energy scales, Phys. Rev. B **93**, 214431 (2016).

[37] S. Sinn, C. H. Kim, B. H. Kim, K. D. Lee, C. J. Won, J. S. Oh, M. Han, Y. J. Chang, N. Hur, H. Sato *et al.*, Electronic structure of the Kitaev material α-RuCl$_3$ probed by photoemission and inverse photoemission spectroscopies, Sci. Rep. **6**, 39544 (2016).

[38] S. Mashhadi, Y. Kim, J. Kim, D. Weber, T. Taniguchi, K. Watanabe, N. Park, B. Lotsch, J. H. Smet, M. Burghard *et al.*, Spin-split band hybridization in graphene proximitized with α-RuCl$_3$ nanosheets, Nano Lett. **19**, 4659 (2019).

[39] T. Gould, S. Lebègue, and J. F. Dobson, Dispersion corrections in graphenic systems: A simple and effective model of binding, J. Phys.: Condens. Matter **25**, 445010 (2013).

[40] X. Zheng, K. Jia, X. Wu, Y. Shi, K. Tanigaki, and R.-R. Du, Tunneling spectroscopic signatures of charge doping and Mott-phase transition in α-RuCl$_3$ in proximity to graphite, arXiv:2205.00409 (2022).

[41] E. Gerber, Y. Yao, T. A. Arias, and E.-A. Kim, *Ab initio* Mismatched Interface Theory of Graphene on α-RuCl$_3$: Doping and Magnetism, Phys. Rev. Lett. **124**, 106804 (2020).

[42] Y. Wang, J. Balgley, E. Gerber, M. Gray, N. Kumar, X. Lu, J.-Q. Yan, A. Fereidouni, R. Basnet, S. J. Yun *et al.*, Modulation doping via a two-dimensional atomic crystalline acceptor, Nano Lett. **20**, 8446 (2020).

[43] B. Zhou, J. Balgley, P. Lampen-Kelley, J.-Q. Yan, D. G. Mandrus, and E. A. Henriksen, Evidence for charge transfer and proximate magnetism in graphene–α-RuCl$_3$ heterostructures, Phys. Rev. B **100**, 165426 (2019).

[44] J. Martin, N. Akerman, G. Ulbricht, T. Lohmann, J. H. Smet, and K. Von Klitzing, Observation of electronhole puddles in graphene using a scanning single-electron transistor, Nat. Phys. **4**, 144 (2008).

[45] R. H. Miwa, T. M. Schmidt, W. L. Scopel, and A. Fazzio, Doping of graphene adsorbed on the a-SiO$_2$ surface, Appl. Phys. Lett. **99**, 163108 (2011).

[46] D.-s. Wang, R. Wu, and A. J. Freeman, First-principles theory of surface magnetocrystalline anisotropy and the diatomic-pair model, Phys. Rev. B **47**, 14932 (1993).

[47] B. S. Yang, J. Zhang, L. N. Jiang, W. Z. Chen, P. Tang, X.-G. Zhang, Y. Yan, and X. F. Han, Strain induced enhancement of perpendicular magnetic anisotropy in Co/graphene

and Co/Bn heterostructures, Phys. Rev. B **95**, 174424 (2017).

[48] Y. Song, X. Wang, and W. Mi, Role of electron filling in the magnetic anisotropy of monolayer WSe$_2$ doped with 5d transition metals, Phys. Rev. Mater. **1**, 074408 (2017).

[49] R. Scherwitzl, P. Zubko, I. G. Lezama, S. Ono, A. F. Morpurgo, G. Catalan, and J.-M. Triscone, Electric-field control of the metal-insulator transition in ultrathin NdNiO$_3$ films, Adv. Mater. **22**, 5517 (2010).

[50] T. Zou, J. Peng, M. Gottschalk, P. P. Zhang, Z. Q. Mao, and X. Ke, Insulator-metal transition induced by electric voltage in a ruthenate Mott insulator, J. Phys.: Condens. Matter **31**, 195602 (2019).

[51] E. Janod, J. Tranchant, B. Corraze, M. Querré, P. Stoliar, M. Rozenberg, T. Cren, D. Roditchev, V. T. Phuoc, M.-P. Besland, and L. Cario, Resistive switching in Mott insulators and correlated systems, Adv. Funct. Mater. **25**, 6287 (2015).

[52] E. S. Souza, W. L. Scopel, and R. H. Miwa, Switchable magnetic moment in cobalt-doped graphene bilayer on Cu (111): An *ab initio* study, Phys. Rev. B **93**, 235308 (2016).

[53] J. E. Padilha, R. H. Miwa, A. J. R. da Silva, and A. Fazzio, Two-dimensional van der Waals p-n junction of inse/phosphorene, Phys. Rev. B **95**, 195143 (2017).

[54] R. B. Pontes, R. H. Miwa, A. J. R. da Silva, A. Fazzio, and J. E. Padilha, Layer-dependent band alignment of few layers of blue phosphorus and their van der Waals heterostructures with graphene, Phys. Rev. B **97**, 235419 (2018).

[55] S. Jiang, J. Shan, and K. F. Mak, Electric-field switching of two-dimensional van der Waals magnets, Nat. Mater. **17**, 406 (2018).

[56] E. S. Morell, A. León, R. H. Miwa, and P. Vargas, Control of magnetism in bilayer CrI$_3$ by an external electric field, 2D Mater. **6**, 025020 (2019).

[57] T. Song, Z. Fei, M. Yankowitz, Z. Lin, Q. Jiang, K. Hwangbo, Q. Zhang, B. Sun, T. Taniguchi, K. Watanabe *et al.*, Switching 2D magnetic states via pressure tuning of layer stacking, Nat. Mater. **18**, 1298 (2019).

[58] D. P. de A. Deus, I. S. S. de Oliveira, J. B. Oliveira, W. L. Scopel, and R. H. Miwa, Magnetic and electronic switch in metal intercalated two-dimensional GeP$_3$, Phys. Rev. Mater. **5**, 054002 (2021).

[59] The external electric field was simulated through the inclusion of a sawlike electric potential, and the atomic positions were fully relaxed within the convergence criterion described in Sec. II (Computational details).

[60] http:/sdumont.lncc.br.